Journal of Atmospheric and Solar-Terrestrial Physics 105-106 (2013) 214–229

Contents lists available at ScienceDirect

Journal of Atmospheric and Solar-Terrestrial Physics

journal homepage: www.elsevier.com/locate/jastp

A multi-beam incoherent scatter radar technique for the estimation of ionospheric electron density and T_e/T_i profiles at Jicamarca

Marco A. Milla [a,*], Erhan Kudeki [b], Pablo M. Reyes [b], Jorge L. Chau [a]

[a] Radio Observatorio de Jicamarca, Instituto Geofísico del Perú, Lima, Peru
[b] Department of Electrical and Computer Engineering, University of Illinois at Urbana-Champaign, Urbana, IL 61801, USA

ARTICLE INFO

Article history:
Received 7 November 2012
Received in revised form
18 June 2013
Accepted 18 June 2013
Available online 28 June 2013

Keywords:
Incoherent scatter
Equatorial ionosphere
Remote sensing

ABSTRACT

A multi-beam incoherent scatter radar technique has been developed at the Jicamarca Radio Observatory in order to maximize the number of ionospheric parameters that can be estimated simultaneously. The technique interleaves radar observations with antenna beams pointing perpendicular and oblique to the Earth's magnetic field. For the estimation of the ionospheric parameters, we have modeled the magnetic aspect angle variations of the signal power and cross-correlation data measured in multiple directions. The data model, formulated in terms of soft-target radar equations, was built based on the theories of incoherent scattering and magneto-ionic propagation. Applying a nonlinear least-squares inversion algorithm, we have succeeded in measuring simultaneously ionospheric electron densities N_e, electron-to-ion temperature ratios T_e/T_i as well as vertical and zonal plasma drifts. In the past, radar users had to choose between either perpendicular-to-**B** or oblique modes, thus, the application of this technique extends the current capabilities of the Jicamarca radar.

1. Introduction

In this paper, we present a multi-beam incoherent scatter radar technique developed at the Jicamarca radio observatory for the estimation of equatorial F-region plasma parameters. The technique explores the idea of diversifying the modes of radar observation in an attempt of maximizing the number of physical parameters that can be estimated simultaneously. For this purpose, the Jicamarca antenna array was divided into sections that were phased to point into multiple directions such that different incoherent scattering and magnetoionic propagation regimes were probed. In the technique presented here, the antenna beams are configured to point west, east, and south of the local zenith. While the west and east beams are aimed perpendicular to the Earth's magnetic field **B**, the south beams are pointed at ~4° from the perpendicular-to-**B** direction.

In this multi-beam technique, the data collected with the antenna beams pointed perpendicular to **B** (west and east beams) are used to estimate vertical and zonal plasma drifts at F-region altitudes. These parameters are determined with high accuracy from the Doppler shifts of the very narrow frequency spectra that are typically measured at these pointing directions. The spectral fitting approach used for the drift estimation is well known and it was developed about a decade ago by Kudeki et al. (1999).

In addition to plasma drifts, we can also estimate electron densities N_e and electron-to-ion temperature ratios T_e/T_i using the incoherent scatter data collected not only with the perpendicular-to-**B** (east and west) beams but also with the off-perpendicular (south) beams. The estimation of these parameters is possible after modeling the magnetic aspect angle variations of the signal power and cross-correlation data collected in different directions. Some samples of the measured data are presented in Section 2. The model of these measurements is built based on the theories of incoherent scattering and magnetoionic propagation (e.g., Kudeki and Milla, 2012). The incoherent scatter theory is considered to account for the magnetic aspect angle dependence of the ionospheric radar cross-section (RCS) at heights where the electron temperature exceeds the ion temperature (i.e., when $T_e > T_i$). On the other hand, the magnetoionic theory is considered to model the changes in polarization experienced by the propagating radar signals that depend on the relative orientation between the propagation direction and the ambient magnetic field. While, the fields propagating perpendicular to **B** experience Cotton–Mouton effects, the fields propagating about a degree from this direction are effectively in the Faraday rotation regime. The details of the forward model and inversion procedure developed for the estimation of electron density profiles corrected for the variations of

* Corresponding author. Tel.: +51 1 3172313.
E-mail addresses: marco.milla@jro.igp.gob.pe (M.A. Milla), erhan@illinois.edu (E. Kudeki), pmreyes2@illinois.edu (P.M. Reyes), jorge.chau@jro.igp.gob.pe (J.L. Chau).

1364-6826/$ - see front matter © 2013 Elsevier Ltd. All rights reserved.
http://dx.doi.org/10.1016/j.jastp.2013.06.003

T_e/T_i throughout the bottom-side of the F-region are discussed in Section 3. The development of this technique was motivated by the work of Milla and Kudeki (2006) and can be considered, in some sense, an extension of the procedures developed by Farley (1969), Shypnev (2004), and Kudeki et al. (2003).

Finally, the results obtained with the multi-beam technique, maps of electron densities and T_e/T_i ratios, are presented and described in Section 4. The quality of the fitting results is also analyzed based on the goodness-of-fit criterion. Moreover, our density estimates are compared to ionosonde measurements carried out simultaneously at Jicamarca. This comparison shows an excellent agreement between both set of measurements, result that to some extent validates the application of the incoherent scatter model presented here.

2. Multi-beam radar modes and measurements

The Jicamarca incoherent scatter radar operates at a frequency of 50 MHz near the city of Lima in Peru. Its main antenna consists of two orthogonal arrays of half-wave dipoles placed one on top of the other and labeled as “up” and “down”. The polarizations of these arrays are approximately parallel to the northeast and southeast directions, respectively. The modularity of the Jicamarca antenna facilitates the implementation of a variety of configurations.

Two particular radar configurations were tested in order to study the performance of the multi-beam approach. These radar configurations are referred to as the 3Ba and 3Bb modes (three-beam modes). In each of these modes, different sections of the Jicamarca array were phased to point into three different directions (west, east, and south of the local zenith). We configured two independent antenna sub-arrays for each pointing direction, making a total of six antenna reception channels. The details of the antenna configurations corresponding to the 3Ba and 3Bb modes are given in Appendix A.

In a first data acquisition campaign, the Jicamarca radar was operated in the 3Ba mode between June 16 and 19, 2008. Radar experiments in the 3Bb mode were conducted in two subsequent campaigns, from June 23 to 24, 2008, and also from January 9 to 12, 2009. Despite the differences between antenna configurations, the radar system was operated with the same transmission and reception parameters in these campaigns (see Table 1). In the experiments, radar observations of the upper atmosphere were conducted alternating between perpendicular-to-**B** and off-perpendicular beams. Radar pulses were delivered in sequences that started with 128 pulses transmitted with the west and east (perpendicular-to-**B**) beams followed by 32 pulses transmitted with the up-polarization of the south (off-perpendicular) beams. The repetition frequency of the radar pulses was 150 Hz. The antenna voltages were sampled every 5 km recording a total of 198 range gates per channel per pulse. The radar voltages of consecutive radar sequences were then used to compute self- and cross-power spectrum estimates (see Appendix B for further details).

Table 1
Radar operating parameters considered in the 3Ba and 3Bb experiments.

Radar parameter	West–East	South
Inter-pulse period	1000 km	1000 km
Pulse width	45 km	45 km
Pulse code	3-baud Barker	3-baud Barker
Number of pulses	128	32
Sampling rate	5 km	5 km
Number of samples	198	198

In Fig. 1, we present sample plots of the self- and cross-power spectrum measurements carried out at Jicamarca while operating in the 3Ba and 3Bb modes. The top panels correspond to the data obtained in the 3Ba experiment of June 19, 2008, and the bottom panels correspond to the 3Bb experiment of January 9, 2009. The data presented in these plots were obtained after five minutes of incoherent integration. In each row, the first and second plots are the self-spectra of the signals collected with one pair of antenna beams (i.e., with either the west, east, or south beams). In addition, the third and fourth plots are the magnitude and phase of the corresponding cross-spectrum. Note that the magnitude of the cross-spectrum is normalized by the square root of the product of the associated self-spectra (i.e., the plot corresponds to the magnitude of the coherence spectrum).

In the plots, we can appreciate that the spectra measured with the west and east beams have narrow frequency bandwidths, which is expected for radar observations with antenna beams pointed perpendicular to **B** (e.g., Kudeki et al., 1999; Sulzer and González, 1999). Note that the magnitude of the associated cross-spectrum measurements also have narrow shapes. As mentioned before, the Doppler shifts of the spectra measured with the west and east beams are used to determine vertical and zonal plasma drifts with high accuracy (which is mainly due to the sharpness of the spectra). On the other hand, we can also see in Fig. 1 that the spectra measured with the south beams, which are pointed off-perpendicular to **B**, are very flat. The reason for this is that the bandwidth of the off-perpendicular radar signal is greater than the pulse-to-pulse sampling frequency (which in this case is 150 Hz). Therefore, the measured spectra are aliased. In addition, note that the signals collected with the south beams experience Faraday rotation effects. As these beams are orthogonally polarized, we can see how the polarization of the backscattered signal rotates, i.e., how power signal goes from one polarization to the other as the radar range increases. These effects will be discussed in more detail later in this section.

The frequency components of the self- and cross-power spectrum measurements are summed to obtain signal power and cross-correlation profiles. In Fig. 2, we present range vs. time plots of the power and correlation data measured in the 3Ba experiment of June 19, 2008. In the left column, power data collected with all the radar beams are displayed in linear scale. Additionally, cross-correlation data of the three pairs of antenna beams are presented in the right column. The magnitude of the correlation is displayed in linear scale, while the phase is plotted in degrees.

In these plots, we can observe marked differences between the power and correlation measured with the perpendicular-to-**B** (west and east) beams and with the off-perpendicular (south) beams. As discussed in the literature (e.g., Budden, 1961; Kudeki and Milla, 2012), radiowaves propagating through the ionosphere experience changes in their polarizations due to the presence of the Earth's magnetic field. The magneto-ionic theory is the basis to study and model these polarization variations which are dependent on the particular modes of propagation excited by the wave fields. As the characteristics of these modes vary with magnetic aspect angle, power and correlation profiles measured at different pointing directions will have, to some extent, distinct shapes. In our discussion, we consider the magnetic aspect angle as the complement of the angle between the propagation direction and the geomagnetic field.

When the beam is pointed (at least one degree) away from perpendicular to **B**, the modes excited by the beam are effectively in the Faraday rotation regime. In this regime, the polarization of a linearly polarized wave rotates as it propagates. This behavior can be observed in the power plots of the orthogonally polarized south-beams, where, power from one polarization goes to the other as the radar range increases. Note that a minimum of power

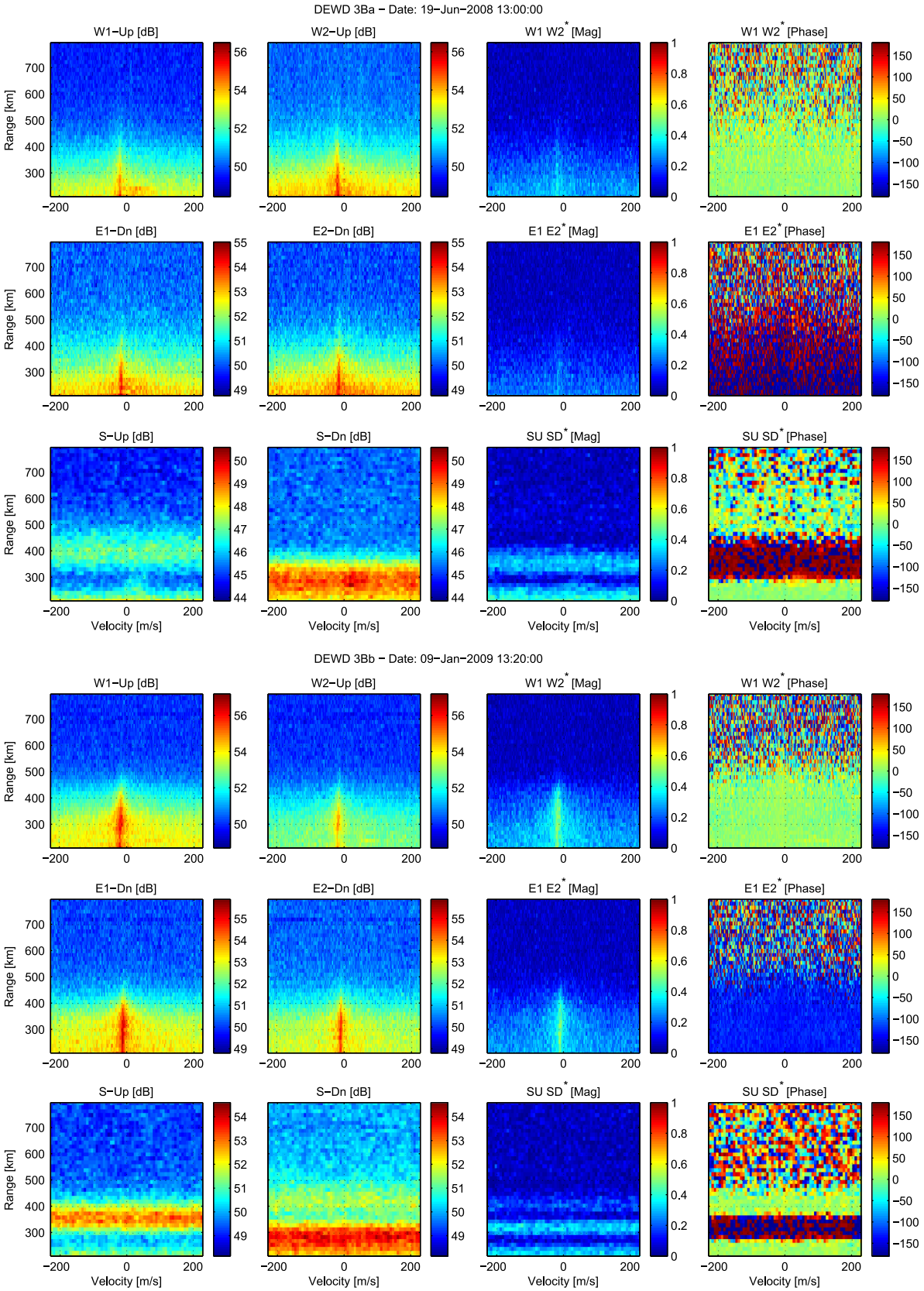

Fig. 1. Sample self- and cross-spectra measured in the 3Ba experiment of June 19, 2008 (top rows), and in the 3Bb experiment of January 9, 2009 (bottom rows). The sample data were obtained after five min of integration. The self- and cross-spectra are plotted as functions of Doppler velocity and radar range.

in one polarization corresponds to a maximum in the other and that the transition between consecutive minimum and maximum values in a power profile corresponds to a 90° rotation of the polarization of the detected field. Faraday rotation effects can also be observed in the cross-correlation plots. The transition between consecutive minimum values in a profile of the magnitude of the

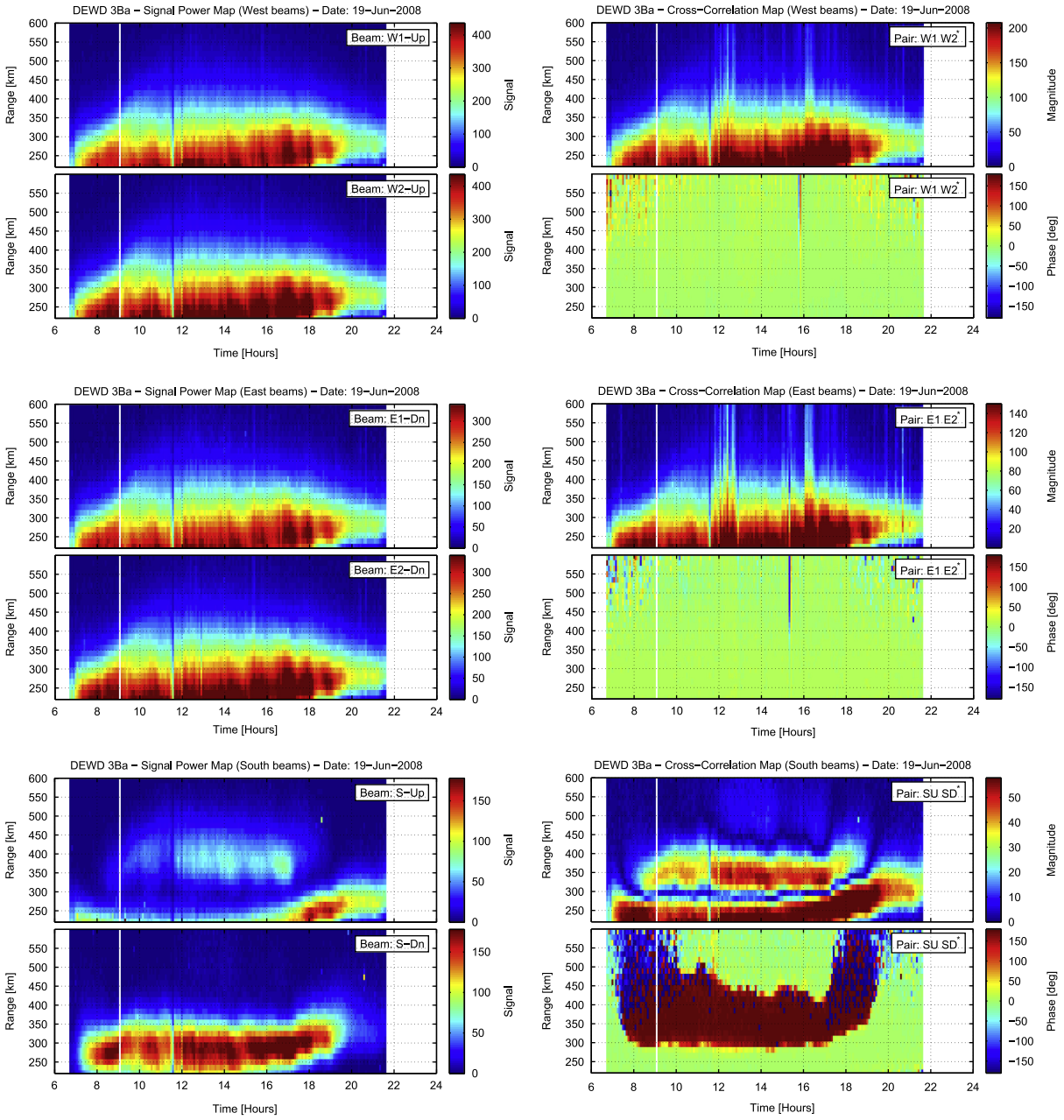

Fig. 2. Range vs. time plots of the signal power and cross-correlation data measured in the 3Ba experiment of June 19, 2008. On the left, power data collected by each of the radar beams are displayed in linear scale. On the right, magnitudes of the cross-correlation data are plotted in linear scale and the associated phases are plotted in degrees.

cross-correlation, coincident with sudden changes in the correlation phase, is related to a 180° rotation of the polarization vector.

As it is well known, around the perpendicular-to-**B** direction, the modes of magneto-ionic propagation vary quite rapidly from the Cotton–Mouton regime at exact perpendicularity to the Faraday rotation regime at aspect angles around and greater than one degree (e.g., Farley, 1969; Yeh et al., 1999). Since the perpendicular-to-**B** (west and east) beams in the 3Ba (and also in the 3Bb) experiments have widths of the order of a degree, the signals collected with these beams are the result of the combination of different modes of propagation. This complicates the description of the measurements. Although there are no apparent signatures of Faraday rotation in the power plots of the west and east beams, some fraction of power actually "rotates." However, this fraction of the returned power is not detected by the receiving arrays as the pair of west (and also east) beams are co-polarized.

In addition, note that, in the 3Ba mode, the west beam arrays, as well as the east beam arrays, constitute radar interferometers aligned in the east–west direction. Using the correlation and power data obtained with these interferometers, we have computed coherence profiles and noticed that the corresponding magnitudes and phases are constant in height—a result that was expected, as it is discussed next. The coherence measured by a radar interferometer (assuming a beam-filling scattering process) is a sample of the spatial Fourier transform of the effective antenna beam shape along the direction of the interferometer baseline. On the other hand, due to magneto-ionic propagation effects, the effective antenna beam shape vary in the direction in which the magnetic aspect angle changes, which in our case correspond to the north–south direction. Since the beam pattern is not modified in the east–west direction, the coherence measured by the interferometer should remain the same at different heights. Therefore,

in this case, magneto-ionic propagation does not play a role in the determination of the coherence. This has been verified with the measurements, as coherence values are equal at all radar ranges. We also noted that the magnitudes of the coherences are approximately equal to the theoretical values (presented in the previous section, see Fig. A2). This result gives us confidence that the actual shapes of the radar beams are very close to the theoretical patterns.

Similar plots, but for the data measured in the 3Bb experiment of January 9, 2009, are presented in Fig. 3. In general, the features of the power and correlation measurements presented in these plots are similar to the features of the 3Ba measurements displayed in Fig. 2. However, there are some differences that need to be pointed out. First, note that the power measured with one of the west beams is stronger than the power detected by the other beam. A similar difference can be observed between the signals collected with the east beams. The reason for these differences is that the antennas constituting each pair are of different sizes, one of them is twice as large as the other (see the description of the antenna configurations in the previous section). On the other hand, note that the west- and east-beam pairs are also radar interferometers, but the antennas are now aligned in the north–south direction. In this case, we expect that magneto-ionic propagation effects will have an impact on the cross-correlation profiles measured with these interferometers, as observed in similar experiments (e.g., Feng et al., 2004). However, the measurements show that the phase of the correlation is almost constant as function of height. Although altitudinal changes of

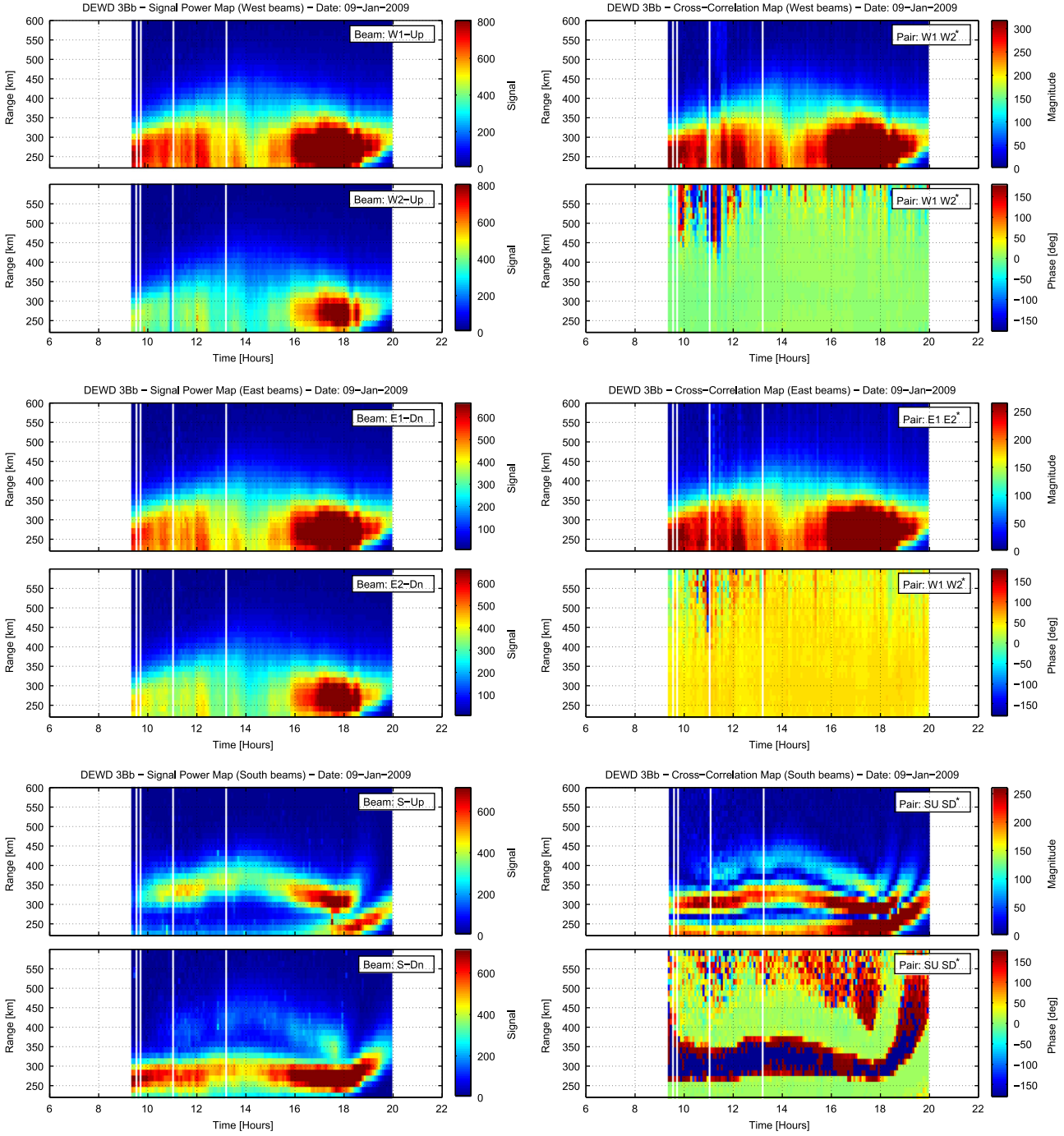

Fig. 3. Same plots as described in Fig. 2, but for the signal power and cross-correlation data measured in the 3Bb experiment of January 9, 2009.

the phase were expected, the lack of variations can be attributed to the following two reasons. First, note that, due to solar minimum conditions, the ionospheric densities in the years of 2008 and 2009 are smaller than typical values; thus, magneto-ionic effects on perpendicular-to-**B** measurements were relatively weak during these experiments. On top of that, note that the separation between the interferometric antennas is not as large as in the 3Ba configuration. Since phase variations are directly proportional to the separation between antennas, the 3Bb north–south interferometers is less sensitive to magneto-ionic effects.

In the following section, the different features of the power and cross-correlation data discussed above are modeled based on incoherent scatter and magneto-ionic propagation theories. The model is then used to invert electron densities and T_e/T_i profiles of the equatorial ionosphere.

3. Data model and inversion technique

In this section, the forward model for the power and cross-correlation data collected in the 3Ba and 3Bb experiments is formulated based on the theories of incoherent scattering and magneto-ionic propagation (e.g., Kudeki and Milla, 2012). In addition, the details of the numerical implementation of the data models are discussed. The inversion technique used for the estimation of the ionospheric parameters is also described and some sample plots of the outcomes of the fitting results are presented.

3.1. Spatial correlation of scattered fields

A transmitter illuminates the ionosphere with electromagnetic pulses of waveform $f(t)$ and carrier wavenumber $k_o = 2\pi/\lambda_o$. In reception, multiple antennas placed at different locations collect the backscattered signals using matched filter receivers. Next, we model the correlation of the voltages detected with a pair of antennas located at positions $\mathbf{d}_i$ and $\mathbf{d}_j$.

In the ionosphere, the random field scattered from an infinitesimal volume $dv = r^2\, dr\, d\Omega$ located at a position $\mathbf{r}$ is dependent on the fluctuating component of the ionospheric electron density. The expected returned power from dv is proportional to the radar cross-section (RCS) $dv\ \int(d\omega/2\pi)\sigma_v(\mathbf{k},\omega)$ where $\sigma_v(\mathbf{k},\omega)$ is the soft-target RCS per unit volume per unit Doppler frequency $\omega/2\pi$ and $\mathbf{k} = -2k_o\hat{\mathbf{r}}$ is the Bragg wave vector. In addition, the phase difference $\psi_{i,j}$ between the fields at $\mathbf{d}_i$ and $\mathbf{d}_j$ is equal to the projection of the wave vector $\mathbf{k}_o = k_o\hat{\mathbf{r}}$ onto the vector difference between the antenna positions, i.e., $\psi_{i,j} = \mathbf{k}_o \cdot (\mathbf{d}_i - \mathbf{d}_j) = \mathbf{k}_o \cdot \mathbf{d}_{i,j}$. Since the voltages detected by the antenna receivers are weighted integrals of wave contributions coming from different directions, we can expressed the cross-correlation of the voltages at the outputs of the i-th and j-th receivers as follows (e.g., Woodman, 1991)

$$\langle v_i(t)v_j^*(t)\rangle = K_{i,j}\int dr\, d\Omega\, \frac{d\omega}{2\pi}\frac{G_t(\hat{\mathbf{r}})A_r(\hat{\mathbf{r}})}{(4\pi r)^2}e^{j\mathbf{k}_o\cdot\mathbf{d}_{i,j}}\left|\chi\left(t-\frac{2r}{c},\omega\right)\right|^2\sigma_v(\mathbf{k},\omega), \tag{1}$$

where t is the radar delay, c is the speed of light, and integrals are taken over range r, solid angle Ω, and Doppler frequency $\omega/2\pi$. The factor $K_{i,j}$ is a cross-calibration constant dependent on gains and losses along the i-th and j-th signal paths. Above, $G_t(\hat{\mathbf{r}})$ and $A_r(\hat{\mathbf{r}})$ are the gain and effective area of the antennas used in transmission and reception. In addition, $\chi(t,\omega)$ is the radar ambiguity function defined as (e.g., Levanon, 1988)

$$\chi(t,\omega) \equiv \frac{1}{T}f(t)e^{j\omega t} * f^*(-t) = \frac{1}{T}\int d\tau\, e^{j\omega\tau}f(\tau)f^*(\tau - t), \tag{2}$$

where T denotes the duration of the pulse waveform $f(t)$.

In Eq. (1), the volumetric radar cross-section spectrum $\sigma_v(\mathbf{k},\omega)$ can be written in the following form:

$$\sigma_v(\mathbf{k},\omega) = 4\pi r_e^2\langle|n_e(\mathbf{k},\omega)|^2\rangle, \tag{3}$$

where r_e is the classical electron radius and $\langle|n_e(\mathbf{k},\ \omega)|^2\rangle$ denotes the space-time spectrum of electron density fluctuations n_e (also known as the incoherent scatter spectrum) which is dependent on the physical parameters of the probed plasma volume (e.g., density, temperatures, composition, etc.). The problem of formulating $\langle|n_e(\mathbf{k},\ \omega)|^2\rangle$ has been worked out by different authors applying different methods. For a review of the problem from an engineering perspective, we refer to the work of Kudeki and Milla (2011) and Milla and Kudeki (2011).

Before introducing magneto-ionic propagation effects into our data model, let us first generalize Eq. (1) by rewriting it in the following form:

$$\langle v_i(t)v_j^*(t)\rangle = K_{i,j}\int dr\, d\Omega\frac{d\omega}{2\pi}\frac{1}{4\pi r^2}W_{i,j}(\hat{\mathbf{r}})\left|\chi(t-\frac{2r}{c},\omega)\right|^2\sigma_v(\mathbf{k},\omega), \tag{4}$$

where $W_{i,j}(\hat{\mathbf{r}})$ is effectively a complex two-way antenna gain given by

$$\begin{aligned} W_{i,j}(\hat{\mathbf{r}}) &= \frac{1}{4\pi}G_t(\hat{\mathbf{r}})A_r(\hat{\mathbf{r}})e^{j\mathbf{k}_o\cdot\mathbf{d}_{i,j}} \\ &= \frac{\lambda_o^2}{16\pi^2}G_t(\hat{\mathbf{r}})G_r(\hat{\mathbf{r}})e^{j\mathbf{k}_o\cdot\mathbf{d}_{i,j}} \end{aligned} \tag{5}$$

expressed in terms of antenna gains provided that $A(\hat{\mathbf{r}}) = (\lambda_o/4\pi)G(\hat{\mathbf{r}})$. Note that this expression is valid as long as the reception antennas are identical. In order to consider antennas of different sizes or shapes, let us express the antenna gain $G(\hat{\mathbf{r}})$ in terms of complex antenna factors $\mathcal{F}(\hat{\mathbf{r}})$ and polarization unit vectors $\hat{\mathbf{p}}(\hat{\mathbf{r}})$ such that

$$G(\hat{\mathbf{r}}) = (\mathcal{F}(\hat{\mathbf{r}})\hat{\mathbf{p}}(\hat{\mathbf{r}}))\cdot(\mathcal{F}(\hat{\mathbf{r}})\hat{\mathbf{p}}(\hat{\mathbf{r}}))^*, \tag{6}$$

expression that satisfies the relation $\int d\Omega G(\hat{\mathbf{r}}) = \int d\Omega|\mathcal{F}(\hat{\mathbf{r}})|^2 = 4\pi$. Making use of these terms, we can rewrite expression 5 as follows:

$$W_{i,j}(\hat{\mathbf{r}}) = \frac{\lambda_o^2}{16\pi^2}|\mathcal{F}_t(\hat{\mathbf{r}})|^2\mathcal{F}_i(\hat{\mathbf{r}})\mathcal{F}_j^*(\hat{\mathbf{r}})\Gamma_{i,j}(\mathbf{r}) \tag{7}$$

where $\mathcal{F}_t(\hat{\mathbf{r}})$, $\mathcal{F}_i(\hat{\mathbf{r}})$, and $\mathcal{F}_j(\hat{\mathbf{r}})$ are the complex antenna factors of the transmitting antenna and i- and j-th receiving antennas. Note that $\mathcal{F}_i(\hat{\mathbf{r}})$ and $\mathcal{F}_j(\hat{\mathbf{r}})$ account for the phase factors $e^{j\mathbf{k}_o\cdot\mathbf{d}_i}$ and $e^{j\mathbf{k}_o\cdot\mathbf{d}_j}$, respectively (as long as they have been computed considering the same reference system). In addition, $\Gamma_{i,j}(\mathbf{r})$ is a cross-polarization factor defined as

$$\Gamma_{i,j}(\hat{\mathbf{r}}) = (\hat{\mathbf{p}}_i(\hat{\mathbf{r}})\cdot\hat{\mathbf{p}}_t(\hat{\mathbf{r}}))(\hat{\mathbf{p}}_j(\hat{\mathbf{r}})\cdot\hat{\mathbf{p}}_t(\hat{\mathbf{r}}))^* \tag{8}$$

where $\hat{\mathbf{p}}_t(\hat{\mathbf{r}})$, $\hat{\mathbf{p}}_i(\hat{\mathbf{r}})$, and $\hat{\mathbf{p}}_j(\hat{\mathbf{r}})$ are the polarization unit vectors of the transmitting and receiving antennas. Note that in the particular case of co-polarized transmitting and receiving antennas $\Gamma_{i,j}(\hat{\mathbf{r}}) = 1$.

The use of expressions (7) and (8) generalizes our radar equation (4). For instance, we can now handle the case of transmitting and receiving antennas having different polarizations. Note that the effect of magneto-ionic propagation on our radar signals is effectively a modification of the wave polarization vector. Therefore, in order to account for such an effect, the only term that needs to be modified in our radar equation is the polarization factor 8.

3.2. Introducing magneto-ionic propagation effects

Let us consider plane wave propagation in an inhomogeneous magnetized ionosphere. To model the electric field of the propagating wave, we can divide the ionosphere in slabs of equal width perpendicular to the propagation direction $\hat{\mathbf{k}}_o$ such that within each slab the physical plasma parameters (as electron density, electron and ion temperatures, and magnetic field) can be considered constants. In this context, the standard Appleton–Hartree equations (for propagation in a uniformly magnetized plasma) can be applied to represent the fields propagating in each slab.

Ignoring for a moment the altitudinal variations of the ionospheric parameters, the transverse component of the plane wave electric field propagating in the $\hat{\mathbf{k}}_o$ direction from the origin to some range r can be expressed as

$$\mathbf{E}(\mathbf{r}) = \underbrace{e^{-jk_o\overline{n}r}[e^{-jk_o\Delta n r}\mathbf{p}_O\mathbf{p}_O^{\mathrm{H}} + e^{jk_o\Delta n r}\mathbf{p}_X\mathbf{p}_X^{\mathrm{H}}]}_{\overline{\mathbf{T}}}\mathbf{E}_o, \tag{9}$$

which is the superposition of the O- and X-modes of magneto-ionic propagation. Above, $\overline{\mathbf{T}}$ denotes a propagator matrix (expressed in cartesian coordinates), where $k_o = \omega_o/c$ is the free-space wavenumber, $\overline{n} = n_O + n_X/2$ and $\Delta n = n_O - n_X/2$ are the mean and half difference between the O- and X-mode refractive indices

$$n_{O/X} = \sqrt{1 - \frac{X}{1 - F_{O/X}}}, \tag{10}$$

specified by the Appleton–Hartree equations (e.g., Budden, 1961), in which

$$F_{O/X} = \frac{Y_T^2 \mp \sqrt{Y_T^4 + 4Y_L^2(1-X)^2}}{2(1-X)}, \tag{11}$$

$$X = \frac{\omega_p^2}{\omega_o^2}, \quad Y_L = \frac{\Omega_e}{\omega_o}\cos\theta, \quad \text{and} \quad Y_T = \frac{\Omega_e}{\omega_o}\sin\theta. \tag{12}$$

Above ω_p and Ω_e are the plasma- and electron gyro-frequencies, respectively, and θ is the angle measured from the magnetic field vector $\mathbf{B}$ to the propagation direction $\hat{\mathbf{k}}_o$.

In Eq. (9), $\mathbf{p}_O$ and $\mathbf{p}_X$ are the polarization vectors of the O- and X-modes defined as

$$\mathbf{p}_O = \frac{\hat{\boldsymbol{\theta}} - ja\hat{\boldsymbol{\phi}}}{\sqrt{1+a^2}} \quad \text{and} \quad \mathbf{p}_X = \frac{-ja\hat{\boldsymbol{\theta}} + \hat{\boldsymbol{\phi}}}{\sqrt{1+a^2}}, \tag{13}$$

where $a = F_O/Y_L = -Y_L/F_X$ is the axial ratio of elliptically polarized modes, and $\hat{\boldsymbol{\theta}}$ and $\hat{\boldsymbol{\phi}}$ are orthogonal unit vectors normal to $\hat{\mathbf{k}}_o$.

Let us extend the previous formulation to the case of an inhomogeneous ionosphere modeled in terms of multiple homogeneous slabs of with Δr. Neglecting reflection from the interfaces between slabs, the field components of an upgoing plane wave propagating in the $+\hat{\mathbf{k}}_o$ direction (at a distance $r_i = i\Delta r$ from the origin) can be computed by the successive application of the propagator matrices (e.g., Feng et al., 2003); that is

$$\mathbf{E}_i^u = \overline{\mathbf{T}}_i \cdots \overline{\mathbf{T}}_2\overline{\mathbf{T}}_1\mathbf{E}_o^u, \tag{14}$$

where $\mathbf{E}_o^u$ is the wave field at the origin (perpendicular to $\hat{\mathbf{k}}_o$), and $\overline{\mathbf{T}}_1 \ldots \overline{\mathbf{T}}_i$ are the propagator matrices from the bottom layer to the i-th layer. Similarly, taking advantage of the bidirectionality of the propagator matrices, the field components of a downgoing plane wave propagating in the $-\hat{\mathbf{k}}_o$ direction (from the i-th layer to the ground) can be written as

$$\mathbf{E}_o^d = \overline{\mathbf{T}}_1\overline{\mathbf{T}}_2 \cdots \overline{\mathbf{T}}_i\mathbf{E}_i^d, \tag{15}$$

where $\mathbf{E}_i^d$ is the field at the top of the i-th layer.

In radar experiments, the transverse field component of the signal backscattered from a radar range $r_i = i\Delta r$ can be modeled as

$$\mathbf{E}_o^r \propto \underbrace{\overline{\mathbf{T}}_1\overline{\mathbf{T}}_2 \cdots \overline{\mathbf{T}}_i\overline{\mathbf{T}}_i \cdots \overline{\mathbf{T}}_2\overline{\mathbf{T}}_1}_{\overline{\boldsymbol{\Pi}}(\mathbf{r}_i)}\mathbf{E}_o^t, \tag{16}$$

where $\mathbf{E}_o^t$ and $\mathbf{E}_o^r$ are the fields transmitted and received by the radar antenna in the $\hat{\mathbf{k}}_o$ direction. Above, $\overline{\boldsymbol{\Pi}}(\mathbf{r}_i)$ denotes a two-way propagator matrix that accounts for the polarization effects on the waves incident on and backscattered from the radar range $\mathbf{r}_i$ (upgoing and downgoing waves, respectively).

Based on the previous description of propagating fields in a magnetized ionosphere, and noticing that the polarization of the fields coming from the range $\mathbf{r}$ is equal to $\overline{\boldsymbol{\Pi}}(\mathbf{r})\hat{\mathbf{p}}_t$, we can reformulate the cross-polarization factor $\Gamma_{i,j}(\mathbf{r})$ introduced in Section 3.1 in the following form:

$$\Gamma_{i,j}(\mathbf{r}) = (\hat{\mathbf{p}}_i^{\mathrm{T}}\overline{\boldsymbol{\Pi}}(\mathbf{r})\hat{\mathbf{p}}_t)(\hat{\mathbf{p}}_j^{\mathrm{T}}\overline{\boldsymbol{\Pi}}(\mathbf{r})\hat{\mathbf{p}}_t)^*. \tag{17}$$

3.3. Power and correlation data models

In order to model the radar measurements collected in 3Ba and 3Bb experiments, we can simplify Eq. (4) assuming that the bandwidth of the incoherent scatter RCS spectrum $\sigma_v(\mathbf{k},\omega)$ is narrower than the frequency response of the matched filters used in reception (a valid approximation in the case of short-pulse radar applications). After integrating over frequency ω, the power of the signal collected by the i-th antenna receiver can be expressed as

$$P_i = \langle |v_i(t)|^2 \rangle = \kappa_i \int dr \frac{|\chi\left(t - \frac{2r}{c}\right)|^2}{4\pi r^2} \int d\Omega\, W_i(\mathbf{r})\sigma_v(\mathbf{k}) + N_i, \tag{18}$$

while the complex cross-correlation of the signals collected by the i-th and j-th receivers can be modeled as

$$C_{i,j} = \langle v_i(t)v_j^*(t) \rangle = \kappa_{i,j} \int dr \frac{|\chi(t - \frac{2r}{c})|^2}{4\pi r^2} \int d\Omega\, W_{i,j}(\mathbf{r})\sigma_v(\mathbf{k}) + N_{i,j}, \tag{19}$$

where we have introduced variables N_i and $N_{i,j}$ to denote the power and cross-correlation of the noise detected by the receivers due to internal or external sources. In these expressions, system calibration constants κ_i and $\kappa_{i,j}$ can take the forms

$$\kappa_i = |g_i|^2 \quad \text{and} \quad \kappa_{i,j} = g_i g_j^*, \tag{20}$$

where g_i and g_j are complex proportionality factors for the voltages detected by the radar receivers.

In Eqs. (18) and (19), the volumetric incoherent scatter RCS $\sigma_v(\mathbf{k})$ is defined as

$$\sigma_v(\mathbf{k}) \equiv 4\pi r_e^2 N_e \eta(\mathbf{k}) \tag{21}$$

where N_e is the electron density and $\eta(\mathbf{k})$ is an electron scattering efficiency factor (see Milla and Kudeki, 2006) given by

$$\eta(\mathbf{k}) \equiv \int \frac{d\omega}{2\pi} \frac{\langle |n_e(\mathbf{k},\omega)|^2 \rangle}{N_e}. \tag{22}$$

This RCS is weighted in range by $\chi(t)$ which is the normalized auto-correlation of the pulse waveform $f(t)$ that can be expressed as

$$\chi(t) = \frac{1}{T} f^*(-t) * f(t), \tag{23}$$

and it is weighted in solid angle by effective two-way antenna gains $W_i(\mathbf{r})$ and $W_{i,j}(\mathbf{r})$ that account for the magneto-ionic propagation effects on the radar signals.

As mentioned before, in the 3Ba and 3Bb experiments, electromagnetic waves are transmitted simultaneously with the antenna arrays pointed in the west and east directions. The west-beam antennas are northeast-polarized, while the east-beam antennas are southeast-polarized. Although these antenna polarizations are

orthogonal, "cross-talk" between the signals collected with these arrays can be generated due to magnetoionic propagation effects. We can model the cross-talk considering that the electric fields detected by a given antenna array can be represented as a linear superposition of the returned fields that would have been measured if the co-polarized and cross-polarized antennas were excited independently.

Denoting the pair of west beams by $w1$ and $w2$ and the pair of east beams by $e1$ and $e2$, the effective two-way antenna gain for the power model (18) can take the following forms:

$$W_{w1}(\mathbf{r}) = \frac{\lambda_o^2}{16\pi^2}|\mathcal{R}_{w1}(\hat{\mathbf{r}})|^2(|\mathcal{T}_w(\hat{\mathbf{r}})|^2\Gamma_u^u(\mathbf{r}) + |\mathcal{T}_e(\hat{\mathbf{r}})|^2\Gamma_u^d(\mathbf{r}) + 2\mathrm{Re}\{\mathcal{T}_w(\hat{\mathbf{r}})\mathcal{T}_e^*(\hat{\mathbf{r}})\Gamma_u^{u,d}(\mathbf{r})\}), \tag{24}$$

$$W_{w2}(\mathbf{r}) = \frac{\lambda_o^2}{16\pi^2}|\mathcal{R}_{w2}(\hat{\mathbf{r}})|^2(|\mathcal{T}_w(\hat{\mathbf{r}})|^2\Gamma_u^u(\mathbf{r}) + |\mathcal{T}_e(\hat{\mathbf{r}})|^2\Gamma_u^d(\mathbf{r}) + 2\mathrm{Re}\{\mathcal{T}_w(\hat{\mathbf{r}})\mathcal{T}_e^*(\hat{\mathbf{r}})\Gamma_u^{u,d}(\mathbf{r})\}), \tag{25}$$

$$W_{e1}(\mathbf{r}) = \frac{\lambda_o^2}{16\pi^2}|\mathcal{R}_{e1}(\hat{\mathbf{r}})|^2(|\mathcal{T}_e(\hat{\mathbf{r}})|^2\Gamma_d^d(\mathbf{r}) + |\mathcal{T}_w(\hat{\mathbf{r}})|^2\Gamma_d^u(\mathbf{r}) + 2\mathrm{Re}\{\mathcal{T}_e(\hat{\mathbf{r}})\mathcal{T}_w^*(\hat{\mathbf{r}})\Gamma_d^{d,u}(\mathbf{r})\}), \tag{26}$$

$$W_{e2}(\mathbf{r}) = \frac{\lambda_o^2}{16\pi^2}|\mathcal{R}_{e2}(\hat{\mathbf{r}})|^2(|\mathcal{T}_e(\hat{\mathbf{r}})|^2\Gamma_d^d(\mathbf{r}) + |\mathcal{T}_w(\hat{\mathbf{r}})|^2\Gamma_d^u(\mathbf{r}) + 2\mathrm{Re}\{\mathcal{T}_e(\hat{\mathbf{r}})\mathcal{T}_w^*(\hat{\mathbf{r}})\Gamma_d^{d,u}(\mathbf{r})\}), \tag{27}$$

while the complex two-way antenna gains for the cross-correlation model (19) can be expressed as

$$W_{w1,w2}(\mathbf{r}) = \frac{\lambda_o^2}{16\pi^2}\mathcal{R}_{w1}(\hat{\mathbf{r}})\mathcal{R}_{w2}^*(\hat{\mathbf{r}})(|\mathcal{T}_w(\hat{\mathbf{r}})|^2\Gamma_u^u(\mathbf{r}) + |\mathcal{T}_e(\hat{\mathbf{r}})|^2\Gamma_u^d(\mathbf{r}) + 2\mathrm{Re}\{\mathcal{T}_w(\hat{\mathbf{r}})\mathcal{T}_e^*(\hat{\mathbf{r}})\Gamma_u^{u,d}(\mathbf{r})\}), \tag{28}$$

$$W_{e1,e2}(\mathbf{r}) = \frac{\lambda_o^2}{16\pi^2}\mathcal{R}_{e1}(\hat{\mathbf{r}})\mathcal{R}_{e2}^*(\hat{\mathbf{r}})(|\mathcal{T}_e(\hat{\mathbf{r}})|^2\Gamma_d^d(\mathbf{r}) + |\mathcal{T}_w(\hat{\mathbf{r}})|^2\Gamma_d^u(\mathbf{r}) + 2\mathrm{Re}\{\mathcal{T}_e(\hat{\mathbf{r}})\mathcal{T}_w^*(\hat{\mathbf{r}})\Gamma_d^{d,u}(\mathbf{r})\}), \tag{29}$$

where λ_o is the radar wavelength. Above, $\mathcal{T}_w(\hat{\mathbf{r}})$ and $\mathcal{T}_e(\hat{\mathbf{r}})$ are the complex antenna factors of the west and east transmitting antennas. In addition, $\mathcal{R}_{w1}(\hat{\mathbf{r}})$, $\mathcal{R}_{w2}(\hat{\mathbf{r}})$, $\mathcal{R}_{e1}(\hat{\mathbf{r}})$, and $\mathcal{R}_{e2}(\hat{\mathbf{r}})$ are the complex antenna factors of the receiving antennas. Note that the products of the forms $|\mathcal{T}_w(\hat{\mathbf{r}})|^2|\mathcal{R}_w(\hat{\mathbf{r}})|^2$ and $|\mathcal{T}_e(\hat{\mathbf{r}})|^2|\mathcal{R}_e(\hat{\mathbf{r}})|^2$ correspond to the two-way radiation patterns displayed in Fig. A2. In the previous equations, the coefficients multiplying the antenna-array factors can be expressed in the following form:

$$\Gamma_{i,j}^{k,l}(\mathbf{r}) = (\hat{\mathbf{p}}_i^{\mathrm{T}}\overline{\mathbf{\Pi}}(\mathbf{r})\hat{\mathbf{p}}_k)(\hat{\mathbf{p}}_j^{\mathrm{T}}\overline{\mathbf{\Pi}}(\mathbf{r})\hat{\mathbf{p}}_l)^*, \tag{30}$$

and represent polarization factors that account for the magnetoionic propagation effects on the returned fields. In addition, $\hat{\mathbf{p}}_i$, $\hat{\mathbf{p}}_j$, $\hat{\mathbf{p}}_k$, and $\hat{\mathbf{p}}_l$ are polarization unit vectors. The indices i and j denote the receiving antennas, while k and l denote the transmitting antennas. In the equations for the effective radiation patterns, these indices are either u for the up-polarization, or d for the down-polarization of the Jicamarca antenna. Furthermore, in order to simplify the notation, we consider the following equivalences $\Gamma_i^k(\mathbf{r})\equiv\Gamma_{i,i}^{k,k}(\mathbf{r})$, $\Gamma_i^{k,l}(\mathbf{r})\equiv\Gamma_{i,i}^{k,l}(\mathbf{r})$, and $\Gamma_{i,j}^k(\mathbf{r})\equiv\Gamma_{i,j}^{k,k}(\mathbf{r})$.

Similarly, denoting the pair of south beams by $s1$ and $s2$, the effective two-way antenna gain for the corresponding power models take the following forms:

$$W_{s1}(\mathbf{r}) = \frac{\lambda_o^2}{16\pi^2}|\mathcal{R}_{s1}(\hat{\mathbf{r}})|^2|\mathcal{T}_s(\hat{\mathbf{r}})|^2\Gamma_u^u(\mathbf{r}), \tag{31}$$

$$W_{s2}(\mathbf{r}) = \frac{\lambda_o^2}{16\pi^2}|\mathcal{R}_{s2}(\hat{\mathbf{r}})|^2|\mathcal{T}_s(\hat{\mathbf{r}})|^2\Gamma_d^u(\mathbf{r}), \tag{32}$$

while the complex two-way antenna gain for the cross-correlation model can be expressed as

$$W_{s1,s2}(\mathbf{r}) = \frac{\lambda_o^2}{16\pi^2}\mathcal{R}_{s1}(\hat{\mathbf{r}})\mathcal{R}_{s2}^*(\hat{\mathbf{r}})|\mathcal{T}_s(\hat{\mathbf{r}})|^2\Gamma_{u,d}^u(\mathbf{r}). \tag{33}$$

Above, $\mathcal{T}_s(\hat{\mathbf{r}})$ is the complex antenna factor of the transmitting array that is up-polarized, while $\mathcal{R}_{s1}(\hat{\mathbf{r}})$ and $\mathcal{R}_{s2}(\hat{\mathbf{r}})$ are the antenna factors of the receiving antennas that are up- and down-polarized, respectively.

In the power and correlation equations presented above, the volumetric RCS $\sigma_v(\mathbf{k})$ and the propagator matrix $\overline{\mathbf{\Pi}}(\mathbf{r})$ are the only functions that depend on ionospheric physical parameters. RCS $\sigma_v(\mathbf{k})$ depends mainly on electron density N_e, temperature ratio T_e/T_i, and magnetic aspect angle α, while $\overline{\mathbf{\Pi}}(\mathbf{r})$ only depends on the electron density and the ambient magnetic field. We are taking advantage of this dependence in order to invert profiles of ionospheric parameters from the data collected in the 3Ba and 3Bb experiments.

3.4. Numerical implementation of data models

As mentioned before, we have considered the ionosphere to be horizontally stratified. The electron density profile $N_e(z)$ is represented as a piecewise linear function

$$N_e(z) = \sum_{l=1}^{L} N_e^l \Delta\left(\frac{z-z_l}{\Delta z}\right) \tag{34}$$

for $z \geq z_1$, where $\Delta(t)$ is the standard triangular function

$$\Delta(t) = \begin{cases} 1-|t| & |t|<1 \\ 0, & \text{otherwise.} \end{cases} \tag{35}$$

The density values at the nodes z_l are $N_e^l = N_e(z_l)$. The nodes are spaced every $\Delta z = 15$ km (which is the length of the baud of the Barker code used in transmission). We have considered $z_1 = 210$ km and $z_L = 600$ km, thus $L=27$. The density profile below z_1 is also modeled by line segments considering a node at $z_0 = 150$ km with density N_e^0 and assuming that below $z = 85$ km the electron density vanishes. In addition, the temperature ratio profile $T_e(z)/T_i(z)$ is modeled as a single layer with a Gaussian shape

$$T_e(z)/T_i(z) = T_m \exp\left(-\frac{(z-z_T)^2}{2w_T^2}\right) + 1, \tag{36}$$

where the constraint $T_e/T_i \geq 1$ is implemented by default. This profile is characterized by the following parameters: $T_m + 1$ is the peak of the temperature ratio, z_T is the altitude where T_e/T_i peaks, and w_T is the width of the Gaussian profile. Modeling the temperature ratio profile as a single layer can be considered a valid approximation for the range of altitudes probed in these experiments. Typical measurements of equatorial ionospheric temperatures (with other radar techniques at Jicamarca) show that, at daytime hours, there is a layer in the bottom-side of the F-region where $T_e/T_i \geq 1$. In order to determine the magnetic field values at different positions from the radar, which is needed by our forward model, we have used the International Geomagnetic Reference Field (IGRF) model (e.g., Olsen et al., 2000).

In order to evaluate the range integrals in the data model formulas, we have discretized Eqs. (18) and (19) to calculate modeled power and cross-correlation samples at range gates $r_n = n\Delta r$ where n is an integer and $\Delta r = 15$ km. In this context, Eqs. (18) and (19) can be recast as discrete convolutions taking the following forms:

$$P_i[n] = |g_i|^2|\chi[n]|^2 * \left(\frac{1}{4\pi r_n^2}\int d\Omega\, W_i(\mathbf{r}_n)\sigma_v(\mathbf{k})\right) + N_i \tag{37}$$

and

$$C_{i,j}[n] = g_i g_j^* |\chi[n]|^2 * \left(\frac{1}{4\pi r_n^2} \int d\Omega \, W_{i,j}(\mathbf{r}_n) \sigma_v(\mathbf{k}) \right) + N_{i,j}, \tag{38}$$

where

$$\chi[n] = \frac{1}{M} c[-n] * c[n] \tag{39}$$

is the discrete auto-correlation of the code $c[n]$ of length M. In our 3Ba and 3Bb experiments, the radar pulses were modulated by a 3-baud Barker sequence ++ − with a baud length equal to 15 km; thus, $c[n] = [1, 1, -1]$ and $M = 3$. In this case, it can be verified that $\chi[n]$ is given by

$$\chi[n] = -\tfrac{1}{3}\delta[n+2] + \delta[n] - \tfrac{1}{3}\delta[n-2]. \tag{40}$$

Furthermore, in order to numerically evaluate the solid angle integrals in (37) and (38), we reformulate the integrals in terms of θ_x and θ_y, which are direction cosines of a coordinate system in which the x- and y-axes are aligned with the local east and north directions (see Figs. A2 and A3). Note that the differential solid angle $d\Omega$ becomes $d\theta_x \, d\theta_y / \sqrt{1-\theta_x^2-\theta_y^2}$. Using this coordinate system, we can take advantage of the magnetic aspect angle dependence of the functions $W_i(\mathbf{r}_n)$, $W_{i,j}(\mathbf{r}_n)$, and $\sigma_v(\mathbf{k})$. As we know, these functions vary quite rapidly in the north–south direction, but very slowly in the east–west direction. Therefore, values of these functions are computed in a grid that is finely sampled in the θ_y−direction with a separation between samples of 0.002 direction cosine units (~0.11°), and coarsely sampled in the θ_x−direction with a separation of 0.113 direction cosine units (~6.5°). A range of approximately $\pm 20^\circ$ with respect to the antenna on-axis direction is covered in both θ_x- and θ_y−directions. The grid is composed of 349 nodes in θ_y and 7 nodes in θ_x; thus, in order to calculate the integrals, a total of 2443 samples are computed for every function. A finite-element-like integration method based on rectangular elements is used to evaluate the solid angle integrals. Note that the same operation has to be repeated for every range gate.

3.5. Data inversion procedure

A trust-region approach for minimizing non-linear least-squares problems subject to simple inequality conditions (e.g., Coleman and Li, 1996) was used for the inversion of our power and cross-correlation data. In comparison with the standard Levenberg–Marquardt algorithm, the trust-region method is more robust for large-scale problems. Additionally, the algorithm allows us to impose lower and upper bounds on the solution of the problem. The following list of parameters are fitted using this minimization algorithm:

- Electron densities N_e^l at the nodes z_l for $0 \le l \le L$.
- Temperature ratio parameters T_m, z_T, and w_T.
- Calibration factors g_i for the six antenna channels.
- Noise power levels N_i for the six antenna channels.
- Noise cross-correlation values $N_{i,j}$ for the three pairs of antenna channels.

Note that g_i and $N_{i,j}$ are complex numbers.

The parameters listed above are estimated by minimizing the following cost function:

$$\mathcal{E}^2 = \mathcal{E}^2_{w1,w2} + \mathcal{E}^2_{e1,e2} + \mathcal{E}^2_{s1,s2}, \tag{41}$$

where

$$\mathcal{E}^2_{i,j} = \sum_n \delta\mathbf{m}_{i,j}^{\mathrm{T}}[n] \overline{\mathbf{M}}_{i,j}^{-1}[n] \delta\mathbf{m}_{i,j}[n] \tag{42}$$

is the error cost function of the data collected with the i-th and j-th antenna channels. In this expression, $\delta\mathbf{m}_{i,j}[n]$ is the vector of differences between the measured and modeled data at the radar range r_n that is defined as

$$\delta\mathbf{m}_{i,j}[n] = \begin{bmatrix} \delta P_i[n] \\ \delta P_j[n] \\ \delta R_{i,j}[n] \\ \delta Q_{i,j}[n] \end{bmatrix} = \begin{bmatrix} p_i[n] - P_i[n] \\ p_j[n] - P_j[n] \\ r_{i,j}[n] - R_{i,j}[n] \\ q_{i,j}[n] - Q_{i,j}[n] \end{bmatrix}, \tag{43}$$

where $p_i[n]$ and $p_j[n]$ denote the power measurements, and $r_{i,j}[n]$ and $q_{i,j}[n]$ correspond to the real and imaginary parts of the cross-correlation data. In addition, $P_i[n]$, $P_j[n]$, $R_{i,j}[n] = \mathrm{Re}\{C_{i,j}[n]\}$, and $Q_{i,j}[n] = \mathrm{Im}\{C_{i,j}[n]\}$ are the modeled power (37) and cross-correlation (38). In the cost function (42), $\overline{\mathbf{M}}_{i,j}[n]$ is the covariance matrix of the vector of data measurement errors $\delta\mathbf{m}_{i,j}[n]$, i.e., $\overline{\mathbf{M}}_{i,j}[n] = \langle \delta\mathbf{m}_{i,j}[n] \delta\mathbf{m}_{i,j}^{\mathrm{T}}[n] \rangle$. Assuming that $\delta\mathbf{m}_{i,j}[n]$ is a zero-mean Gaussian random vector, $\overline{\mathbf{M}}_{i,j}[n]$ can be written in the following form (e.g., Feng et al., 2004):

$$\overline{\mathbf{M}}_{i,j} = \frac{1}{I} \begin{bmatrix} P_i^2 & R_{i,j}^2 + Q_{i,j}^2 & P_i R_{i,j} & P_i Q_{i,j} \\ R_{i,j}^2 + Q_{i,j}^2 & P_j^2 & P_j R_{i,j} & P_j Q_{i,j} \\ P_i R_{i,j} & P_j R_{i,j} & \frac{1}{2}(R_{i,j}^2 - Q_{i,j}^2 + P_i P_j) & R_{i,j} Q_{i,j} \\ P_i Q_{i,j} & P_j Q_{i,j} & R_{i,j} Q_{i,j} & \frac{1}{2}(Q_{i,j}^2 - R_{i,j}^2 + P_i P_j) \end{bmatrix}, \tag{44}$$

where I is the number of samples used to compute the power and cross-correlation data. In this expression, indices n were omitted in order to simplify the notation. The assumption of a Gaussian vector $\delta\mathbf{m}_{i,j}[n]$ can be justified because every element of $\delta\mathbf{m}_{i,j}[n]$ results from the average of a large number of nearly uncorrelated samples. Note that in the cost function (42), we have only considered samples that are spaced every 15 km and that the sum is taken over the set of data between 210 km and 600 km. This implies that 27 range gates (for $14 \le n \le 40$) were fitted.

The form of Eq. (42) is fully valid only if measurements at different range gates are not correlated. Although the decoding procedure generates correlated samples at neighboring range gates, we are using this expression assuming that samples spaced at least a distance equal to the resolution of the pulse shape (which is 15 km) should be weakly correlated. In order to include the oversampled data in our inversion procedure, a more complicated cost function has to be considered because the data corresponding to neighboring gates spaced every 5 km are definitely correlated. The implementation of the inversion algorithm including the oversampled data will be the subject of future work.

In order to estimate the parameters listed above, we apply the following two-step strategy.

First step:

- Initial values for the electron density, noise, and calibration parameters are determined. In this step, it is assumed that $T_e/T_i = 1$ at all heights.
- The following constraints are specified: electron densities N_e^l and noise levels N_i must be positive, and g_{w1}, g_{e1}, and g_{s1} must be real and positive. The rest of the parameters are not constrained.
- The trust-region method is used to minimize the cost function (41) subject to the constraints specified above. In this first step, we only fit for N_e^l, N_i, $N_{i,j}$, and g_i.

Second step:

- The estimated parameters obtained in the first step are used as an initial guess. In addition, we define initial values for T_m, z_T, and w_T.

- The same constraints specified in the first step are considered in this one. Additionally, the T_e/T_i parameters are restricted to be positive.
- The trust-region method is used again to minimize the cost function (41) but including in the minimization the T_e/T_i parameters. In this second step, we solve for all the parameters listed above, i.e., N_e^l, T_m, z_T, w_T, N_i, $N_{i,j}$, and g_i.

We apply the two-step strategy because we notice that the inversion of $N_e{}^l$ is more robust than the inversion of the T_e/T_i parameters. When fitting directly for the densities and the T_e/T_i parameters all together in a single step, the solutions for T_e/T_i tend to be erratic, which is probably related to the fact that the power and cross-correlation data is somewhat less dependent on T_e/T_i than on the densities. Estimating the only densities in a first step and subsequently the densities plus the T_e/T_i parameters provides better results. Note that we have not considered any explicit regularization term in the cost function (41). However, modeling the T_e/T_i profile as a Gaussian function (characterized with a few parameters) regularizes, in some sense, the problem because a continuity condition on the T_e/T_i profile is imposed.

In Fig. 4, sample plots of the results obtained from the inversion of the 3Ba and 3Bb data are displayed. In these plots, the estimated electron density and T_e/T_i profiles are presented in the left column. In the other columns, the power and cross-correlation measurements (dotted points) are compared with the modeled data profiles resultant from the inversion (continuous lines). We can appreciate that the comparison is good, because measured and modeled data match closely; however, there are some discrepancies (particularly in the cross-correlation data of the south-beams of the 3Ba experiment) that might be related to a poor characterization of the bottom part of the density profile. Further analysis and discussion regarding the characteristics of the results are presented in the following section.

4. Results and comparisons

In Fig. 5, we present plots of the electron density and T_e/T_i estimates obtained from the inversion of incoherent scatter power and cross-correlation data collected in the 3Ba experiment of June 19, 2008 (left column), and also in the 3Bb experiment of January 9, 2009 (right column). To obtain these results, the data model and fitting technique described in the previous sections were applied. Both the N_e and T_e/T_i profiles are plotted in linear scale. First, note that the estimated densities and temperature ratios are within the ranges of values expected for an equatorial ionosphere. Electron densities of the order of 10^{11} m^{-3} are typical of solar-minimum conditions. A layer of $T_e/T_i > 1$ located at the bottom of the F-region is characteristic of the daytime ionosphere. The T_e/T_i layer has peak values greater than two and relaxes toward thermal equilibrium ($T_e = T_i$) as time reaches the nighttime hours. However, we can also observe that the T_e/T_i values fluctuate from one profile to the next one. The origin of these fluctuations is the subject of current analysis. Apparently, the magnitudes of the fluctuations are of the order of the statistical uncertainties expected for these estimates. Note that the radar data collected in the 3Ba and 3Bb experiments can be considered (to some extent) to be less dependent on T_e/T_i than on N_e. As we know, if $T_e/T_i > 1$, the incoherent scatter RCS increases as the magnetic aspect angle α decreases and reaches its maximum value at $\alpha = 0^\circ$ (i.e., at the angle of perpendicular-to-**B** propagation). However, the power increments measured with perpendicular-to-**B** beams are somewhat smaller than the theoretical values for $\alpha = 0^\circ$ because signal contributions with smaller RCS are averaged by the antenna beams. This reduces the sensitivity of the radar data to changes in T_e/T_i. Additionally, note that the fluctuations of the T_e/T_i values are larger in the 3Ba case than in the 3Bb case. This might be related to the fact that the 3Ba two-way radiation patterns are broader in the north–south direction than the 3Bb patterns, thus, a wider range of signal contributions with smaller RCS is collected by the 3Ba beams (see antenna description in Section Appendix A). In addition, note that the incoherent scatter RCS is directly proportional to N_e (see Section 3). Moreover, the altitudinal variations of the measured signals due to magneto-ionic propagation effects are dependent on the electron density values but not on T_e/T_i. Although it is likely that the T_e/T_i fluctuations are due to the statistical errors of the estimated parameters, further studies need to be carried out in order to fully identify the origin of these fluctuations.

In the density plots, we can observe patches of enhanced densities resembling “bead” shapes. Whether these beads were artifacts of the inversion procedure need to be analyzed. First, we examined if these events were correlated with fluctuations on the transmitted power. After analyzing records of the line voltage supplied to the transmitters used in these experiments, we did not find any correlation between the fluctuations of the line voltages and the patches of enhanced electron density. We also noted that the voltage fluctuations follow closely the variations of the radar calibration parameters presented in Fig. 6. As there are no systematic variations that may be the cause for the density increments, we consider the origin of the density beads to be geophysical. Whether these variations are due to solar activity or due to perturbations of the neutral atmosphere will be the subjects of future investigations.

It is also important to describe the characteristics of the radar calibration constants resulting from the inversion of the radar data. Note in Fig. 6 that the calibration constants of the west and east antenna channels exhibit approximately the same variations in time. This is expected if we assume that the only system parameter that may fluctuate during the operation of the radar is the amount of transmitted power. However, we can observe that the features of the calibration parameters of the south channels do not follow necessarily the time variations of the calibration parameters of the other channels. The fact that two different transmitters were used in these experiments (one for the west and east beams and the other for the south beams) might be the reason for the distinct behaviors of the calibration parameters. However, we can also see that the behaviors of the calibration constants of the south beams are somewhat different from each other (particularly in the case of the 3Ba data). These differences become more evident at time intervals in which the electron temperature is greater than the ion temperature (i.e., $T_e/T_i > 1$). The cause for these unexpected differences might be related to a poor description of the electron density profile at altitudes below 200 km where the electron density is low and may have steep altitude gradients (this segment of the density profile is characterized by a single parameter, as explained in Section 3). The shape of the lower part of the electron density profile determines the amount of Faraday rotation that the south-beam fields experience up to the first altitude of the data samples used in our inversions. If a simplified description of the bottom part of the density profile is causing an inaccurate estimation of these parameters, the use of ionosonde data on the inversion of the lower part of the density profile might be needed to properly model the radar data and improve the quality of the inversions. Further testing and analysis is needed in order to identify the origin of the differences between the calibration parameters.

In Fig. 7, goodness-of-fit values obtained from the inversion of the 3Ba and 3Bb radar data are presented and can be used to

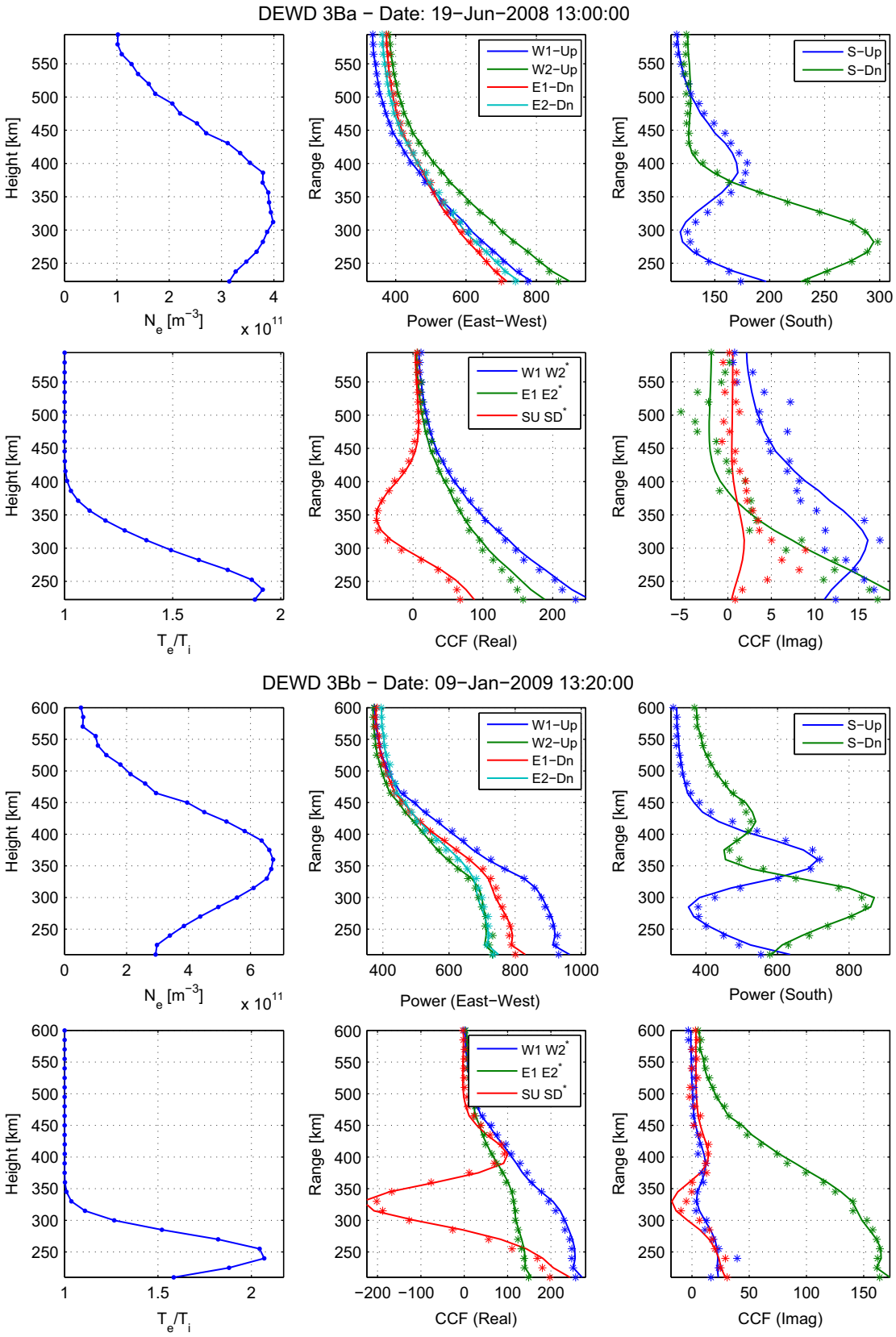

Fig. 4. Sample plots of the results obtained from the inversion of the 3Ba and 3Bb data (top and bottom panels, respectively). The estimated N_e and T_e/T_i profiles are plotted in the left column. In the other columns, the power and cross-correlation measurements (dotted points) are compared with the modeled profiles (continuous lines).

analyze the quality of the inversion results. The goodness-of-fit is defined as $\mathcal{E}^2/N_{\text{measurements}}$. In the plots, the blue curves correspond to the values obtained by fitting only for the electron density N_e and assuming that $T_e/T_i = 1$ at all altitudes. The green curves correspond to the values obtained by fitting for both parameters, N_e and T_e/T_i. The goodness-of-fit values are around five in the case

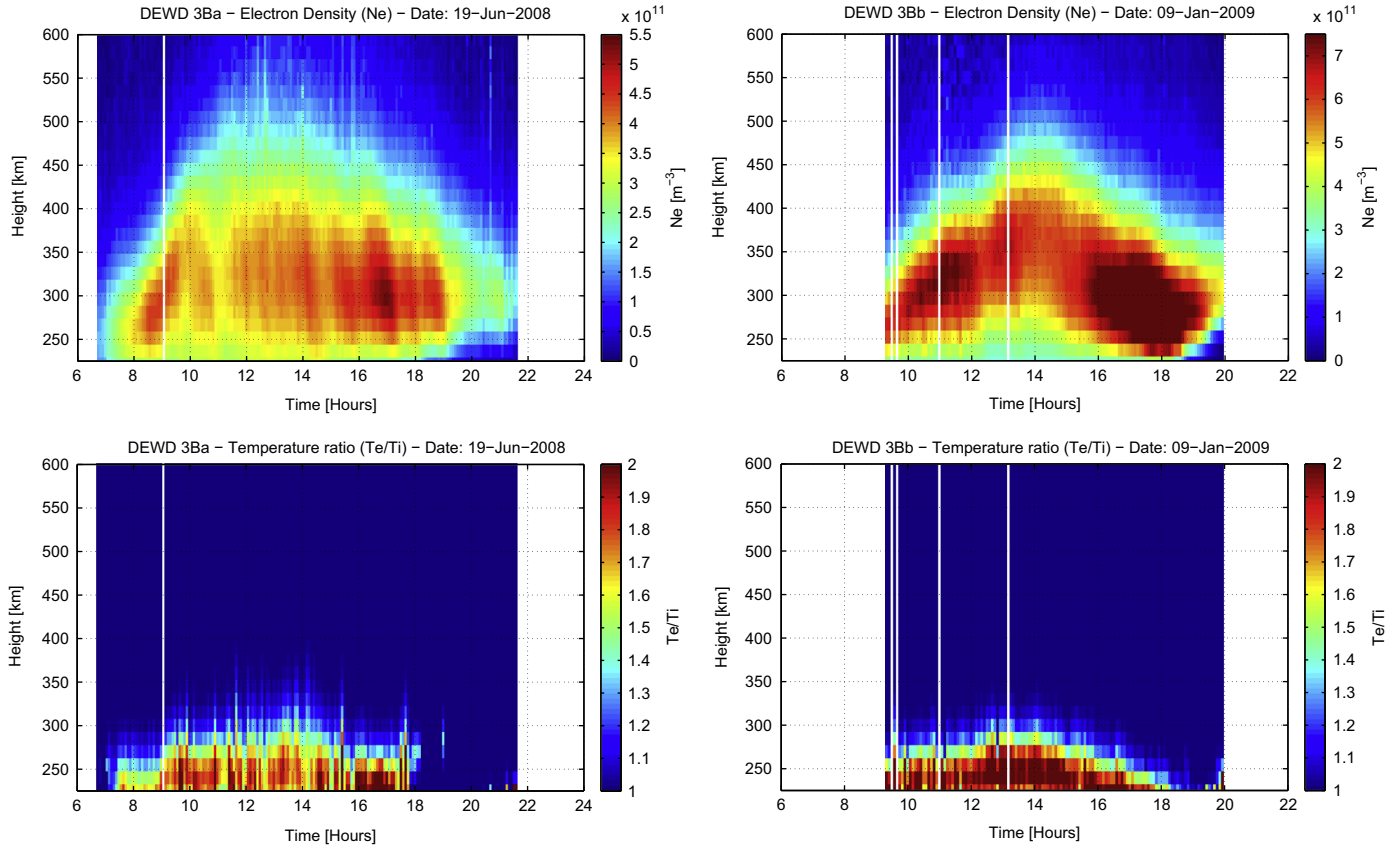

Fig. 5. Range vs. time plots of the electron density and T_e/T_i estimates obtained from the inversion of incoherent scatter signal power and cross-correlation data collected in the 3Ba experiment of June 19, 2008 (left column), and also in the 3Bb experiment of January 9, 2009 (right column).

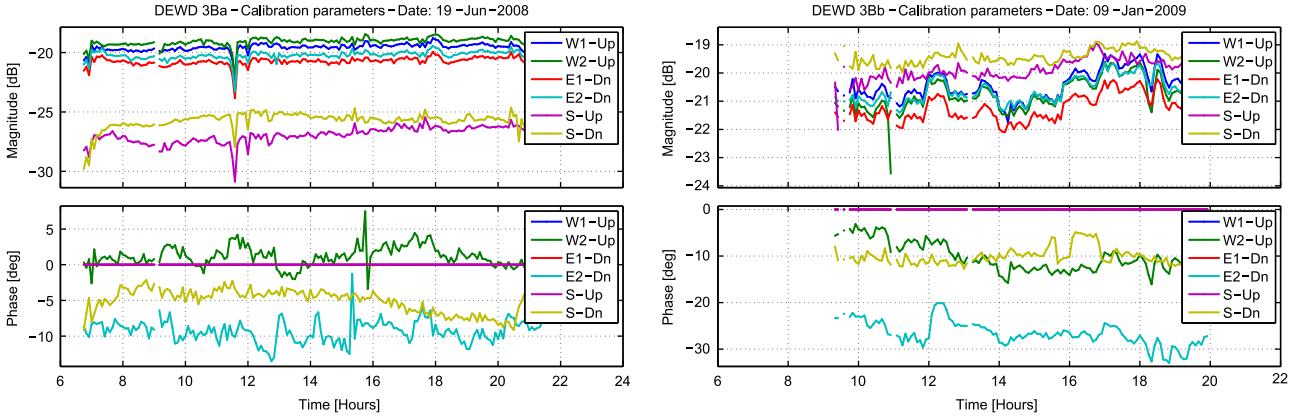

Fig. 6. Magnitudes and phases of the radar calibration constants obtained as part of the inversion of the 3Ba and 3Bb radar data.

of the 3Ba results, while they are around three in the case of the 3Bb results. As expected, note that the goodness-of-fit values are smaller when both ionospheric parameters, N_e and T_e/T_i, are fitted, implying that T_e/T_i correction is needed. However, the goodness-of-fit values obtained are, in some sense, somewhat large, because a "good" fitting result corresponds to a goodness-of-fit value close to one. This indicates that the model has not totally captured the features of the data; therefore, there is still space for improvement.

In addition, in order to validate our estimated densities, we have compared our results with ionosonde measurements conducted simultaneously at Jicamarca. In Fig. 8, we are comparing the peak values of the plasma frequencies (foF2 $= 1/2\pi\sqrt{N_e e^2/m_e\epsilon_o}$) measured with the 3Ba and 3Bb radar techniques (blue points) and with the ionosonde measurements (red points). In addition, the altitudes corresponding to the peak values of the plasma frequencies are compared in Fig. 9. Although the ionosonde data is noisy in the 3Ba case, we can observe that the agreement is very good, particularly in the 3Bb case. Note that the oscillations on the plasma frequency curves are correlated with the patches of enhanced densities described before. The fact that the same behavior can be observed in both radar and ionosonde measurements reinforces our conclusion that the origin of these patches is geophysical.

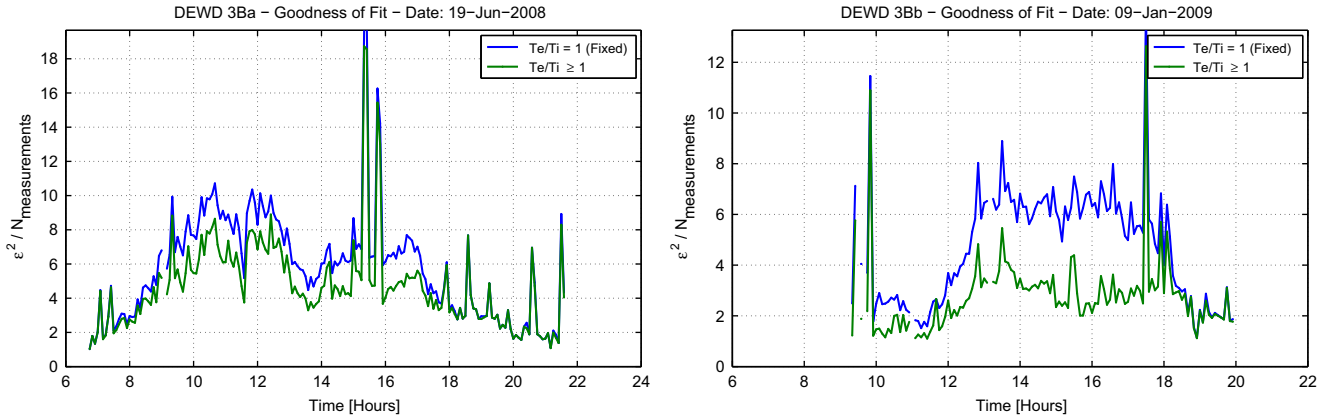

Fig. 7. Goodness-of-fit values resulting from the inversion of the 3Ba and 3Bb radar data. The blue curves correspond to the values obtained by fitting only for the electron density N_e and assuming that $T_e/T_i = 1$ at all altitudes. The green curves correspond to the values obtained by fitting for both parameters, N_e and T_e/T_i. (For interpretation of the references to color in this figure caption, the reader is referred to the web version of this article.)

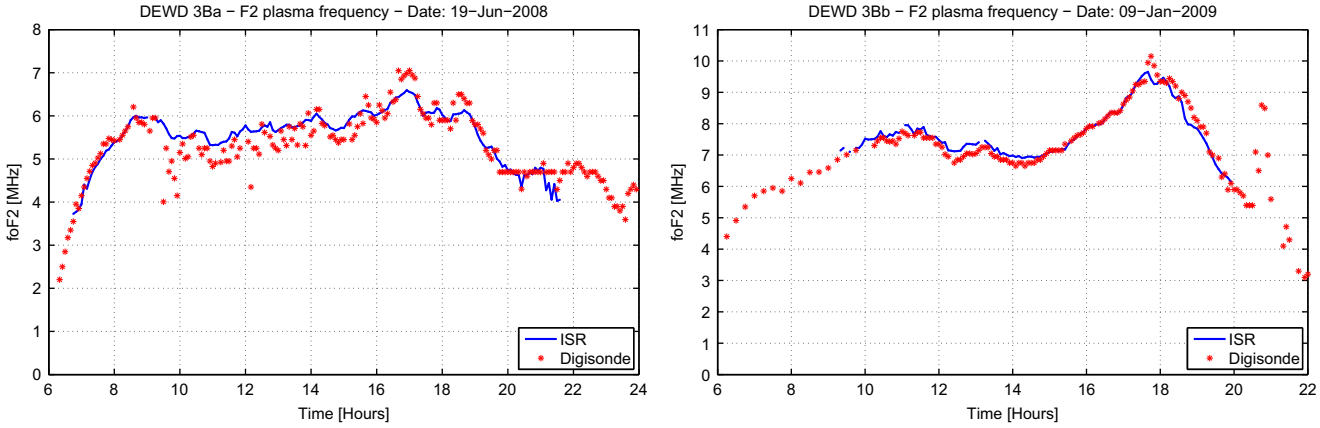

Fig. 8. Comparison of the peak values of plasma frequencies (foF2) measured with the 3Ba and 3Bb radar techniques (blue lines) and with an ionosonde system also located at Jicamarca (red dots). (For interpretation of the references to color in this figure caption, the reader is referred to the web version of this article.)

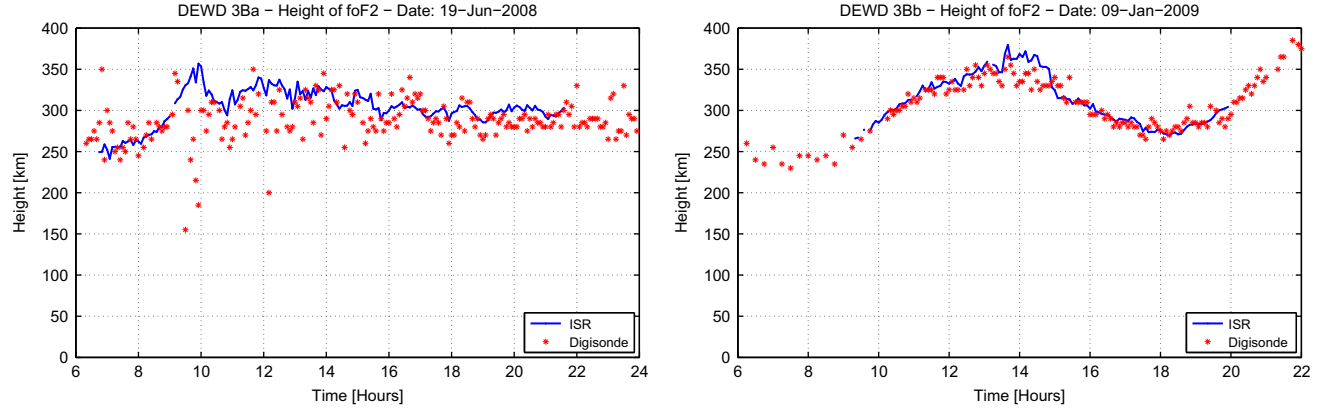

Fig. 9. Comparison of the altitudes corresponding to the peak values of plasma frequency presented in Fig. 8.

5. Summary

In this paper, we have presented a detailed description of a multi-beam incoherent scatter radar technique developed for the estimation of ionospheric plasma parameters using the Jicamarca radar. Two particular antenna configurations that divide the Jicamarca array in sections too point into three different directions (3Ba and 3Bb modes) were considered in the experiments conducted to test this technique. As discussed before, the 3Ba and 3Bb modes have succeed in estimating simultaneously electron densities, electron-to-ion temperature ratios, as well as, vertical and zonal plasma drifts. In addition to these physical parameters, radar calibration factors were also obtained as outcomes of the inversion procedure and can be used to diagnose the integrity of the radar system. The quality of our inversion results were analyzed based on the goodness-of-fit criterion. We have

also verified that the electron density estimates obtained with our technique are in excellent agreement with ionosonde measurements that were carried out simultaneously at Jicamarca. Although the quality of our estimated parameters can be considered good, a more careful analysis of their associated statistical errors is left as a future work. Moreover, as discussed in the previous section, there are certain features in our estimated results that will be the subject of further investigations.

Appendix A. Antenna configuration

The antenna configurations used in the 3Ba and 3Bb experiments are displayed in Fig. A1. In the 3Ba mode, the Jicamarca antenna is configured as follows:

- West Beam 1: West quadrant of up-polarization.
- West Beam 2: East quadrant of up-polarization.
- East Beam 1: West quadrant of down-polarization.
- East Beam 2: East quadrant of down-polarization.
- South Beam 1: South and north quadrants of up-polarization.
- South Beam 2: South and north quadrants of down-polarization.

In the 3Bb mode, the configuration is somewhat different.

- West Beam 1: East and west quadrants of up-polarization (bow-tie antenna).
- West Beam 2: North quadrant of up-polarization.
- East Beam 1: East and west quadrants of down-polarization (bow-tie antenna).
- East Beam 2: North quadrant of down-polarization.
- South Beam 1: South quadrant of up-polarization.
- South Beam 2: South quadrant of down-polarization.

Note that the west beams are co-polarized parallel to the northeast direction (up-polarization) and that the east beams are also co-polarized but parallel to the southeast direction (down-polarization). On the other hand, the south beams are cross-polarized: the first beam is polarized northeast, while the second one is polarized southeast.

The two-way radiation patterns of the radar beams used in the 3Ba and 3Bb experiments are presented in Figs. A2 and A3. The patterns are displayed in dB units (using color scale) as functions of direction cosines, θ_x and θ_y, with respect to the x- and y-axes of a coordinate system in which the antenna is located at the origin. In this coordinate system, the z-axis is perpendicular to the plane of the Jicamarca antenna, and the x- and y-axes are aligned with the local east and north directions (i.e., the coordinate system is rotated 51° positive azimuth with respect to the direction of alignment of the "down" antenna dipoles). In the plots, the black lines trace the loci of magnetic perpendicularity for June 2008 at different altitudes (100, 500, and 1000 km). As indicated earlier in this appendix, the west-beam (as well as the east-beam) sub-arrays of the 3Ba configuration are quarters of the Jicamarca antenna. Also, note that each antenna pair is aligned in the east–west direction. On the other hand, in the 3Bb mode, the sub-arrays of the west-beam (or east-beam) pair are of different sizes and are aligned in the north–south direction. One of the subarrays is still an antenna quarter, but the other is composed of two quarters forming a "bow-tie" array configuration (see Fig. A1). Because of this, we can observe in the right panels of Fig. A2 that the 3Bb west-beam radiation patterns look different from each other. The same can be observed in the case of the east-beam radiation patterns. As we can expect, the bow-tie arrays have narrower beams in the east–west direction. Moreover, their radiation patterns have larger directivities and A_{BS} (backscatter radar aperture) factors, which implies that the data collected by the bow-tie arrays will have better SNR values. In each plot, the values of the expected coherences between the co-polarized signals of the west-beam and east-beam antenna pairs are given. In general, the coherence is ~0.5 (a reference value that is calculated assuming a beam-filling scattering process and disregarding magneto-ionic propagation effects).

In Fig. A3, the two-way radiation patterns of the south beams used in the 3Ba and 3Bb experiments are displayed. Note that, in the north–south direction, the 3Ba south beam is narrower than the 3Bb beam. This is because the south-beam antennas in the 3Ba mode are the combination of two quadrants of the Jicamarca array (the north and south quadrants), but in the 3Bb mode, the antennas are only single quadrants. In addition, note that the A_{BS}

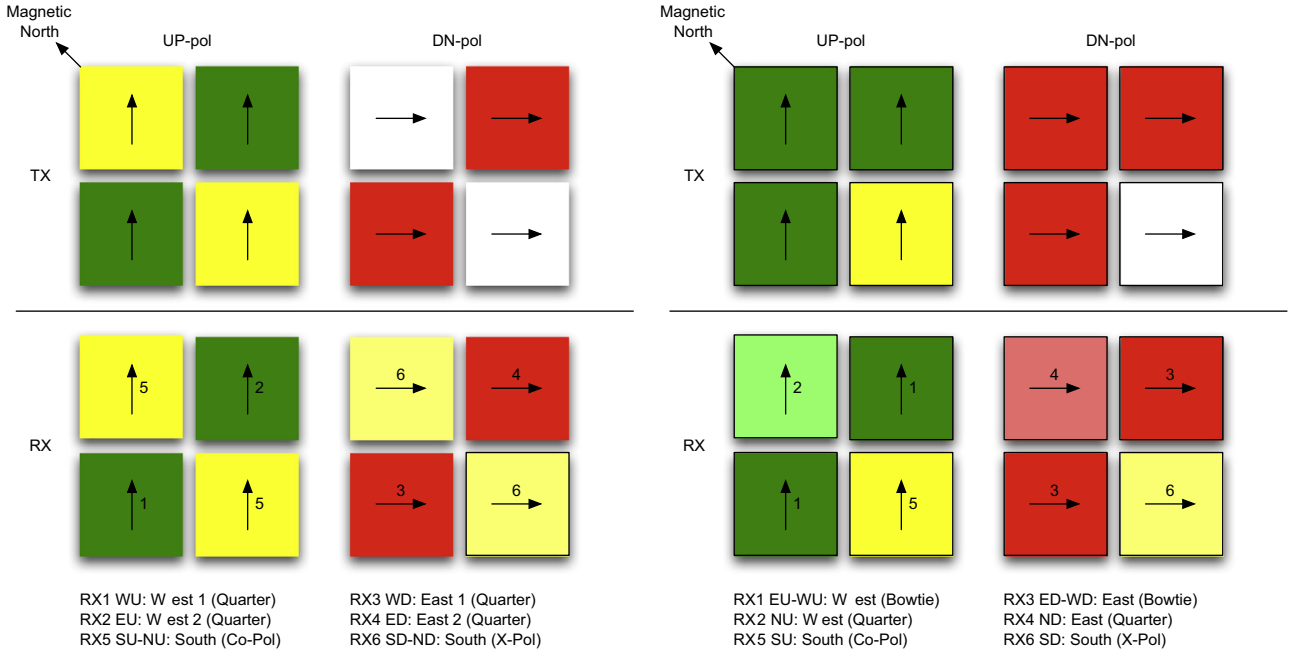

Fig. A1. Antenna configurations of the 3Ba (left panel) and 3Bb (right panel) experiments.

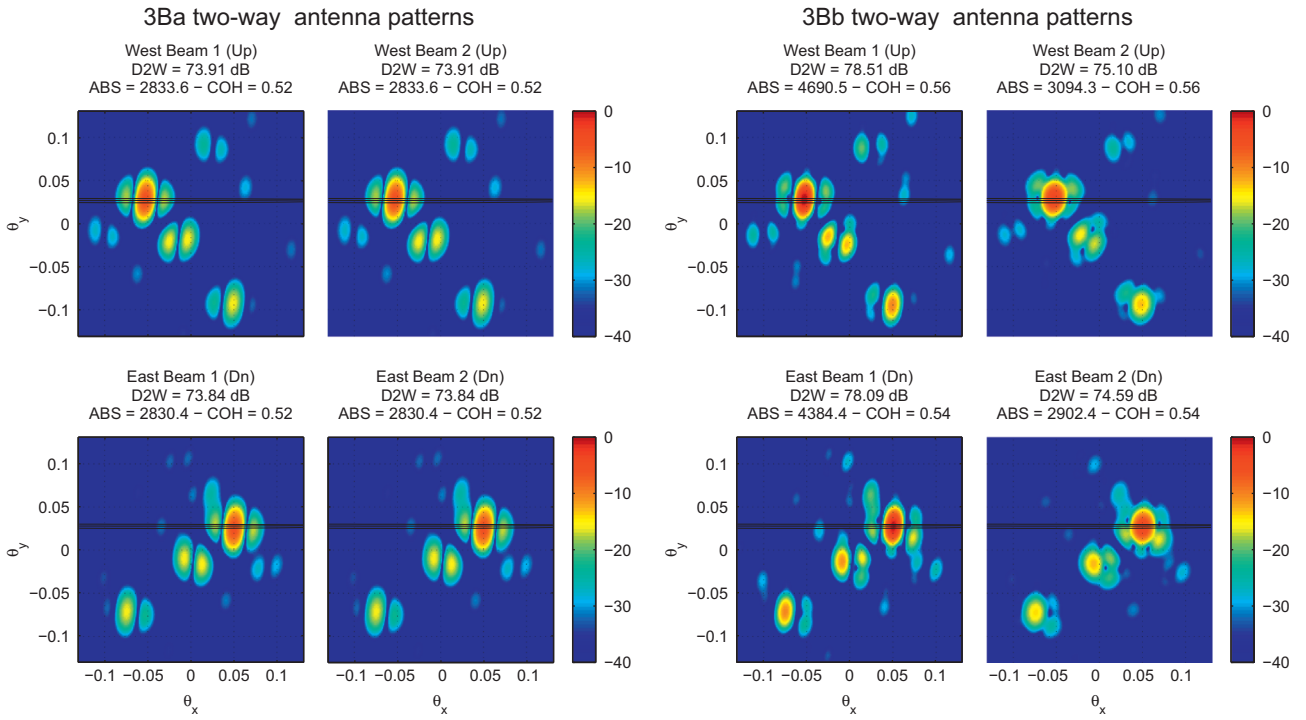

Fig. A2. Two-way radiation patterns of the west (top row) and east (bottom row) beams used in the 3Ba (left) and 3Bb (right) experiments. The patterns are displayed as functions of direction cosines in a coordinate system in which *x*- and *y*-axes are aligned with the east and north directions at Jicamarca. Note that in the 3Ba mode, the patterns of the west beams are identical, but in the 3Bb mode, the west beams have different shapes. The same can be observed in the case of the east beams.

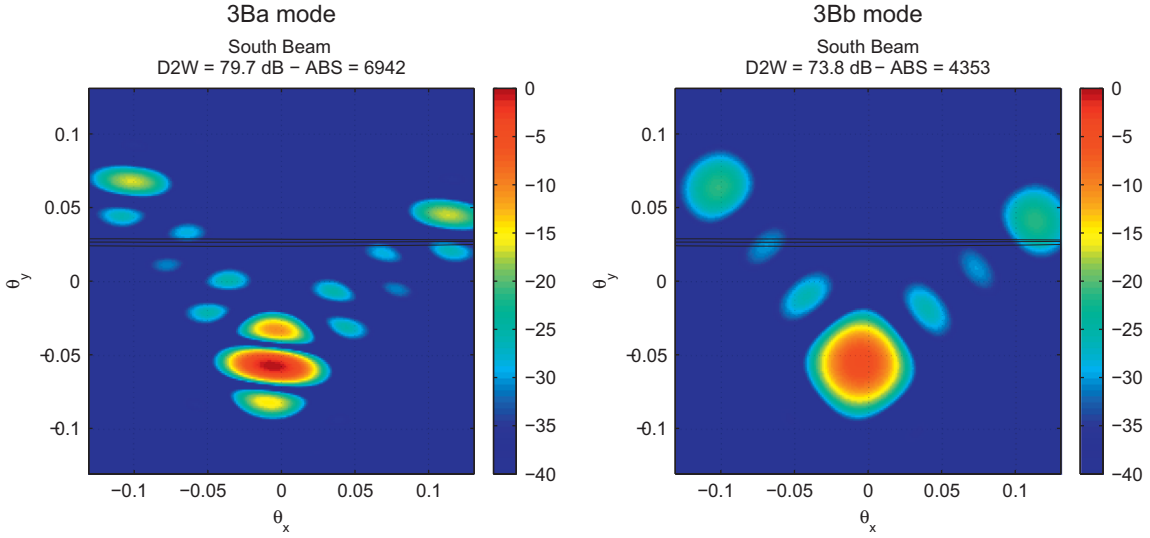

Fig. A3. Two-way radiation patterns of the south beams used in the 3Ba (left) and 3Bb (right) experiments. Note that, in the north–south direction, the 3Ba south-beam is narrower than the corresponding 3Bb beam.

factors of the south beams are in general greater than those of the west and east beams. The reason for this is that the south beams have lower sidelobes than the other beams.

Appendix B. Experiment description

In transmission, electromagnetic wave pulses were delivered in sequences that alternate between perpendicular-to-**B** and off-perpendicular antenna beams. Each sequence started with 128 pulses transmitted with the west- and east-beams (excited simultaneously). These pulses were then followed by 32 pulses transmitted with the up-polarization of the south-beam arrays. The separation between pulses (inter-pulse period or IPP) was 6.667 ms, which is equivalent to a radar range of 1000 km. The length of each transmitted pulse was 45 km. To improve the range resolution, the radar pulses were coded with a 3-baud Barker sequence $++-$ that was flipped every other pulse (the baud length was 15 km). In reception, the backscattered signals coming from the ionosphere were sampled at the antenna outputs using digital receivers. The demodulation and the matched filter detection of the signals are performed numerically in these receivers. Samples of the in-phase and quadrature radar voltages for each antenna channel were obtained every 5 km (i.e., the radar returns

were oversampled by a factor of three with respect to the baud length) sampling a total of 198 range gates.

Using the fast Fourier transform (FFT), time series of the radar voltages collected during each transmission sequence were converted to frequency domain. The computed self- and cross-power spectra have a Nyquist frequency equal to 75 Hz (half of the sampling frequency) which in our case is equivalent to a maximum Doppler velocity of 225 m/s (provided that the radar wavelength is 6 m). The power spectrum estimates obtained in consecutive radar sequences were averaged in order to reduce their statistical uncertainties. Approximately 280 spectra were averaged in 5 min of data integration. The resultant averaged self- and cross-power spectra were processed applying the data model and inversion technique described in Section 3.

References

Budden, K.G., 1961. Radio Waves in the Ionosphere. Cambridge University Press, Cambridge, United Kingdom.

Coleman, T.F., Li, Y., 1996. An interior trust region approach for nonlinear minimization subject to bounds. SIAM Journal on Optimization 6 (May (2)), 418–445.

Farley, D.T., 1969. Faraday rotation measurements using incoherent scatter. Radio Science 4 (February (2)), 143–152.

Feng, Z., Kudeki, E., Woodman, R.F., Chau, J.L., 2003. Transverse-beam incoherent scatter radar measurements of *F*-region plasma densities at Jicamarca. Radio Science 38 (August (4)), 1–11.

Feng, Z., Kudeki, E., Woodman, R.F., Chau, J.L., Milla, M.A., 2004. *F* region plasma density estimation at Jicamarca using the complex cross-correlation of orthogonal polarized backscatter fields. Radio Science 39 (June), 1–8.

Kudeki, E., Bhattacharyya, S., Woodman, R.F., 1999. A new approach in incoherent scatter *F* region $E \times B$ drift measurements at Jicamarca. Journal of Geophysical Research 104 (December (A12)), 28145–28162.

Kudeki, E., Milla, M.A., 2011. Incoherent scatter spectral theories. Part I. A general framework and results for small magnetic aspect angles. IEEE Transactions on Geoscience and Remote Sensing 49 (January (1)), 315–328.

Kudeki, E., Milla, M.A., April 2012. Doppler Radar Observations - Weather Radar, Wind Profiler, Ionospheric Radar, and Other Advanced Applications. InTech, Ch. Incoherent Scatter Radar—Spectral Signal Model and Ionospheric Applications, pp. 377–406.

Kudeki, E., Woodman, R.F., Feng, Z., 2003. Incoherent scatter radar plasma density measurements at Jicamarca using a transverse-mode differential-phase method. Geophysical Research Letters 30 (March (5)), 1255.

Levanon, N., 1988. Radar Principles. Wiley-Interscience, New York, NY.

Milla, M.A., Kudeki, E., 2006. *F*-region electron density and T_e/T_i measurements using incoherent scatter power data collected at ALTAIR. Annales Geophysicae 24 (July (5)), 1333–1342.

Milla, M.A., Kudeki, E., 2011. Incoherent scatter spectral theories. Part II. Modeling the spectrum for modes propagating perpendicular to *B*. IEEE Transactions on Geoscience and Remote Sensing 49 (January (1)), 329–345.

Olsen, N., Sabaka, T.J., Tøffner-Clausen, L., 2000. Determination of the IGRF 2000 model. Earth Planets and Space 52 (December (12)), 1175–1182.

Shypnev, B.G., 2004. Incoherent scatter Faraday rotation measurements on a radar with single linear polarization. Radio Science 39 (May (3)), 1–8.

Sulzer, M.P., González, S.A., 1999. The effect of electron Coulomb collisions on the incoherent scatter spectrum in the *F* region at Jicamarca. Journal of Geophysical Research 104 (October (A10)), 22535–22551.

Woodman, R.F., 1991. A general statistical instrument theory of atmospheric and ionospheric radars. Journal of Geophysical Research 96 (May (A5)), 7911–7928.

Yeh, K.C., Chao, H.Y., Lin, K.H., 1999. A study of the generalized Faraday effect in several media. Radio Science 34 (January–February (1)), 139–153.